Int. J. Electrochem. Sci., 17 **(2022)** Article Number: 221158, doi: 10.20964/2022.11.56

International Journal of
ELECTROCHEMICAL
SCIENCE
www.electrochemsci.org

Study on the Setting and Hardening Process of red mud-coal metakaolin geopolymer concrete by Electrochemical Impedance Spectroscopy

Pan Shen, Pengju Han[*]*, Tiantian Guo, Ruijie Wang, Wei Song, Xiaohong Bai, Fuli Ma,*
Xiaoyuan Wang, Bin He

College of Civil Engineering, Taiyuan University of Technology, Taiyuan, 030024, China
[*]E-mail: 13834569544@163.com

Received: 7 August 2022 / *Accepted:* 27 September 2022 / *Published:* 10 October 2022

The setting and hardening of red mud-coal metakaolin geopolymer concrete (RCGC) was studied. To this end, four sets of RCGC blocks with different water-binder ratios (0.50, 0.55, 0.60, and 0.65) were prepared. The workability, setting time, and compressive strength of four RCGC specimens with different water-binder ratios were evaluated. The electrochemical performance of RCGC was analyzed by electrochemical impedance spectroscopy (EIS), and the process of coagulation and hardening was analyzed through equivalent circuit parameters. X-ray diffraction (XRD), nuclear magnetic resonance (NMR), and scanning electron microscopy-energy dispersive analysis (SEM-EDS) were used to investigate the coagulation and hardening mechanism of RCGC materials. The experimental results show that the increase of the water-binder ratio prolonged the setting time of RCGC and increased the slump. There is a good linear relationship between the compressive strength and the impedance parameters R_s and R_{ct}. Over time, the pores of the material are gradually filled with coagulation and hardening products, and the microstructure is gradually developed.

Keywords: Geopolymer concrete; Electrochemical impedance spectroscopy; Nuclear magnetic resonance test; Compressive strength; Microstructure.

1. INTRODUCTION

In the global construction industry, concrete is the most widely used building material. Among them, Portland cement is one of the raw materials for concrete, and its popularity will remain high into the foreseeable future, but what is troubling is that Portland cement (in terms of its raw materials) requires much energy in its production process [1-2], and the ratio of Portland cement production to carbon dioxide emissions is about 1:1 [3], accounting for 5-7% of total global emissions [4]. Although the benefits it brings to buildings are significant, its production and use are contrary to the low-carbon theme of energy conservation and environmental protection in today's world. Therefore, there is an urgent need to seek a new low-carbon and sustainable building material to reduce the pressures on today's environment.

A geopolymer can account for much solid waste and reduce carbon emissions in the production process and is an alternative green new cementitious material. Geopolymers can be synthesized at room temperature using activators (alkaline and acidic), raw materials rich in silicon, aluminum, and other additives [5]. They are inorganic polymer cementing materials composed of a three-dimensional network structure within. They have many excellent properties, such as: excellent mechanical properties, good durability under special conditions, and good high-temperature resistance [6-7]. Generally, alkaline activators are prepared by mixing sodium silicate, sodium hydroxide, and distilled water [8-9], and common raw materials rich in silicon and aluminum include agricultural and industrial wastes, such as fly ash [10-12], metakaolin [13-14], slag [15-16], red mud [17-18], sugarcane bagasse ash [19], *etc*. Among them, coal metakaolin is an aluminosilicate mineral formed after coal kaolin is calcined at high temperature, with small particle size and high surface energy [20]. Red mud is a waste produced during bauxite processing and production: it has very fine particles and contains aluminum, iron, and traces of silicon [21]. Its mineral composition is complex, and the alkalinity is high [22]. Based on previous studies, fine aggregates (river sand) and coarse aggregates (crushed stone) were added to the raw materials for producing red mud coal metakaolin geopolymers [23], a geopolymer concrete of red mud coal metakaolin was further synthesized at room temperature.

However, the development and application of geopolymer concrete requires to consider and understand the hardening reaction characteristics of the material itself and the composition of hardening products from many aspects. Shaoyun Pu *et al*. [24] explored the hydration characteristics, thermal properties, and microscopic properties of fly ash geopolymers, and found that with prolongation of curing, the strength of fly ash geopolymers increased, and its crystal phase was composed of brushstone, monetite, and merlinite, and the amorphous phase was composed of -Al-O-P-, -Si-O-P-, and Si-O-Al-O-P- units. Siqi Zhou et al. [25] evaluated the mechanical properties, setting time, and rate of expansion of geopolymers prepared with different ratios of pozzolan and metakaolin. The results showed that the mechanical strength increased with the content of metakaolin. The flow curve of all pastes fitted the Bingham model. Most studies have not explored the agglomeration and hardening mechanisms of geopolymers in depth, and the reaction process of geopolymers is often of significance to its performance and durability.

In addition, the setting and hardening reaction process of geopolymer concrete is a continuous, dynamic process. At present, there are many test methods available to study the hardening characteristics of geopolymer concrete, but many of these methods are destructive. The method of detection is difficult to apply to the whole life cycle monitoring of geopolymers, and its complex reaction process brings considerable technical challenges to the whole cycle detection. Therefore, electrochemical impedance spectroscopy (EIS) has been mooted as a new detection method. EIS is a technical method that uses the input alternating current signal and output signal to study the electrochemical information of the target. It has the advantages of simple operation, high sensitivity, and low cost, and has achieved good results in its application to cement-based materials [26-27].

Based on previous studies, this study explored the workability, setting time, compressive strength and electrochemical characteristics of geopolymer concrete with four water-binder ratios, and a set of water-binder ratios will be selected through the test results, and the mineral composition, and micro-morphology of geopolymer concrete with this water-binder ratio were characterized by scanning electron microscope-energy dispersion spectroscopy(SEM-EDS) , X-ray diffraction(XRD) , and nuclear magnetic resonance(NMR) , and the setting and hardening mechanism of geopolymer concrete was discussed. The results of the study will help to evaluate the development of red mud coal metakaolin geopolymer concrete (RCGC) in future construction applications.

2. TEST MATERIALS AND METHODS

2.1. Material

(1) Red mud (RM) and coal metakaolin (CMK) required for the preparation of geopolymer concrete: The red mud in this experiment was taken from an aluminum plant in Hejin, Shanxi Province, China, and was grinded to 74 μm and dried. The coal metakaolin was produced by an industry and trade company from Xinzhou, Shanxi Province, China. It was a white powdery hard metakaolin with high activity. The main components of the RM and CMK are displayed in Table 1.

Table 1. Main chemical components of RM and CMK

Raw materials	Ingredient/ wt%										
	SiO_2	Al_2O_3	TiO_2	Fe_2O_3	CaO	MgO	K_2O	Na_2O	CO_2	S	LOI
RM	21.05	27.38	4.04	6.42	14.91	0.53	0.77	11.86	3.90	0.36	8.78
CMK	52.62	45.42	0.85	0.45	0.17	0.11	0.13	0.25	–	–	–

(2) Alkali activator: analytically pure NaOH particles (purity greater than 99.0%), distilled water (prepared by laboratory distillation) and industrial sodium silicate (modulus: 3.12, Baume degree: 40), were mixed in a certain proportion in the test. Among them, the chemical composition of industrial water glass is $Na_2O:SiO_2:H_2O = 1:3.03:8.21$.

(3) Fine aggregate: The sand is ordinary river sand (particle size less than 5 mm).

(4) Coarse aggregate: crushed stone (washed with water, dried, and screened, the particle size is 5-20 mm).

2.2. Sample preparation

A total of four groups of geopolymer concrete blocks with different water-binder ratios (0.50, 0.55, 0.60, and 0.65) were prepared. The mass ratio of red mud and coal metakaolin was 7:3, and they were evenly mixed after weighing. The alkali activator was composed of sodium hydroxide, industrial sodium silicate, and distilled water mixed with Na_2O/H_2O= 23.0. The obtained solution was left to stand and cooled to room temperature before use.

The red mud, coal metakaolin, sand and crushed stone were put into a concrete mixer and stirred for 6 minutes, by slowly adding the alkali activator solution, the mixture was fully stirred for 5 minutes to obtain a RCGC mixture, poured into a cube mold, vibrated on a vibrating table for 5 minutes and vibrated to form: all air bubbles were discharged, and finally the surface of the mold was scraped flat, wrapped with plastic film, and placed in a standard constant-temperature and humidity curing box, under standard curing conditions, the mold is released after curing for one day. There were two types of cube mold: the RCGC samples were prepared in the first (100 mm × 100 mm × 100 mm) for mechanical property evaluation. The second RCGC sample block was prepared in a smaller cube mold (70.7 mm × 70.7 mm × 70.7 mm) for electrochemical testing and analysis.

2.3. Workability test

The workability of concrete is based on the corresponding standard GB/T 50080-2016 [28]. A trumpet-shaped slump bucket with an upper opening of 100mm, a lower opening of 200mm, and a height of 300mm were used to pour the pre-configured geopolymer concrete into 3 layers, and each layer was 1/3 the height of the slump bucket. , inserted and smashed 25 times with an iron rod for each layer to make it dense, then quickly pulled up the bucket, and used a ruler to measure the height difference between the highest point of the concrete after the collapse and the top of the bucket (300mm), which was the slump value.

2.4. Setting time test

The setting time test of concrete is based on the corresponding standard GB/T 50080-2016 [28]. A 5-mm standard sieve was used to screen an appropriate amount of slurry from the RCGC mixture, and then the sieved slurry was poured into the prepared cylindrical mold (ϕ = 160 mm, h = 150 mm), we first poured one-third of the total depth of the slurry, manually tamped the specimen, then poured in another one-third of the sample, tamped it, and then vibrated on a shaking table until no more bubbles appeared on the free surface, and then the sample was covered with a glass plate, and placed at room temperature for testing.

2.5. Compressive strength test

This test uses an electronic universal testing machine (SHT4605, MTS). The compressive strength test of concrete is based on the corresponding standard GB/T 50081-2019 [29], the control mode was set to constant force speed, and the loading speed was 5 kN/s. The average of the three test values was used as the final recorded compressive strength.

2.6. Electrochemical test

The EIS test was conducted using a Wuhan CorrTest electrochemical workstation. As shown in Fig. 1, the two-electrode method was adopted. First, electrodes were placed on both sides of the RCGC sample, and then one end was connected to the working electrode of the workstation, and the other end was connected to the auxiliary electrode of the workstation. The frequency range of the test conditions was 10-1 to 105 Hz, and the alternating current amplitude was 10 mV. To improve the accuracy of the test process, the methods of current deviation and automatic elimination of potential were used. After the test, the RCGC samples were placed in curing box to continue curing. The data obtained by the EIS test were processed and fitted by ZView2 and ZSimDemo3.30d software.

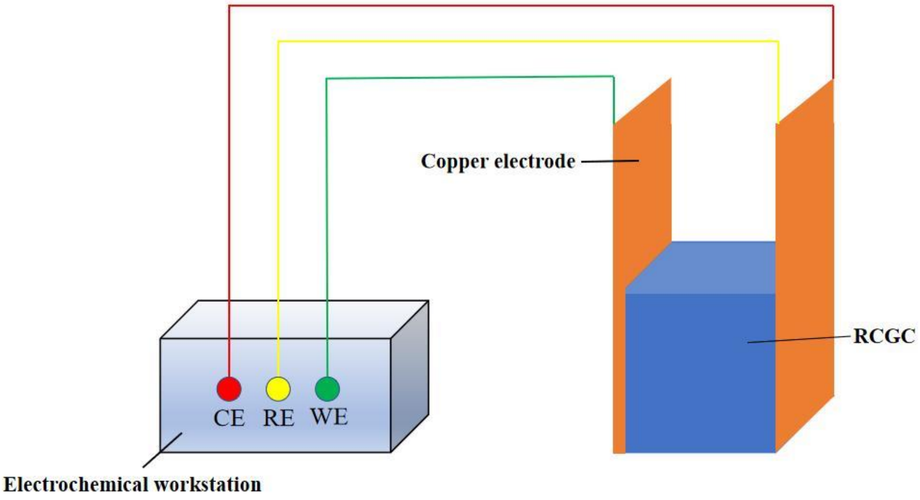

Figure 1. The shematic diagram of EIS test RCGC sample.

2.7. NMR test

Before the test, the RCGC sample block was saturated with water for 24 hours with a vacuum saturator, so that the pores in the RCGC sample block were filled with distilled water. The saturated samples were tested with a Hong 12-150 hydrogen nuclear magnetic resonance pore analyzer (Niumag, China).

2.8. XRD test

The crushed fragments after the compressive strength test were placed in anhydrous ethanol, soaked for 7 days, break the crushed fragments with a wall breaker, and screened through a 0.075-mm square aperture sieve to obtain a powder specimen. A LabX XRD-6000 diffractometer which is from Shimadzu, Japan was used to scan the powdered RCGC samples without interruption for phase testing.

The radiation source was a Cu/Kα target, the scanning ranged from 5° to 60°, in increments of 0.02°, and the scanning speed (measured by diffraction angle) 2θ was 4.0°/min.

2.9. SEM-EDS test

The test samples were taken from the inside of the RCGC block and were formed into RCGC microscopic test samples measuring 15 mm × 15 mm × 5 mm using a cutting machine; the accumulation of negative charges on the surface of the test sample was reduced by gold-spraying treatment. The gold-sprayed samples were pasted onto an aluminum column, and a TM-3000 desktop scanning electron microscope (Hitachi, Japan) was used to obtain micrographs of each specimen and used in conjunction with a Quanta-70 X-ray spectrometer (Bruker, Germany) for energy dispersive analysis.

3. RESULTS AND DISCUSSION

3.1. *Workability*

As shown in Fig. 2, it is the effect of different water-binder ratios during mixing process on RCGC workability. From this figure, it can be seen that the RCGC sample workability is influenced significantly by the water-binder ratios where the increase of additional where the increase of water-binder ratio improves the geopolymer concrete workability. From the test results, the increase in RCGC slump is 102.4%, 143.9% and 163.4% for geopolymer concrete with 0.55, 0.60, and 0.65 water-binder ratio with geopolymer concrete mix with 0.50 water-binder ratio. This improvement in processability is apparently due to an decrease in the water-binder ratio, which greatly decreases the free water content. A similar phenomenon was found in the study by Aliabdo et al. [30].

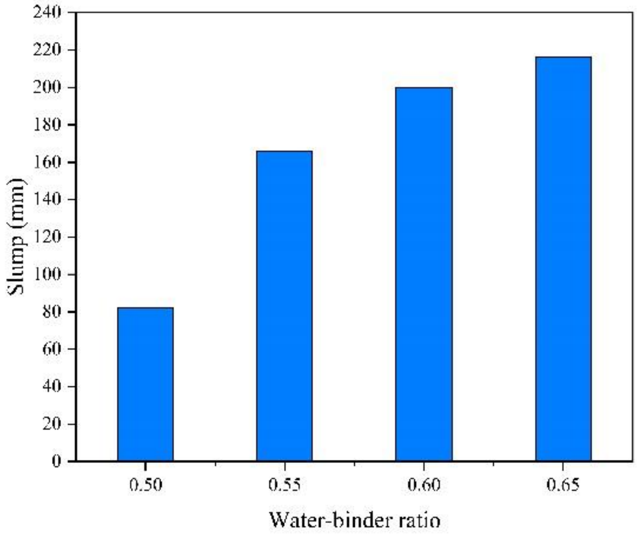

Figure 2. Slump of RCGC samples with four different water-binder ratios(0.50,0.55,0.60, and 0.65).

3.2. Setting time

The results of initial setting times and final setting times of RCGC samples with four water-binder ratios are shown in Fig. 3. The increase of water-binder ratios can reduce the setting time of geopolymer concrete slurry, and the setting time of the slurry continues to decrease with the increasing water-binder ratio. The initial setting times of four water-binder ratios (0.50, 0.55, 0.60, and 0.65) are 480 min, 540 min, 600 min, and 1080 min, the final setting times are 850 min, 900 min, 980 min, and 2160 min. The initial setting time of RCGC slurry samples with three water-binder ratios (0.55, 0.60, and 0.65) are 12.5%, 25.0% and 125.0% longer than that of RCGC slurry samples with water-binder ratio of 0.50, and the final setting time is 5.8%, 15.3%, and 154.1% longer respectively. This is because the increase of the water-binder ratio significantly increases the content of free water in the alkali activator, hence reducing the rate of geopolymerization and prolonging the setting time of the RCGC slurry under the same environment [24]. The results obtained in this study are consistent with other study by Cabezaa et al. [31]。

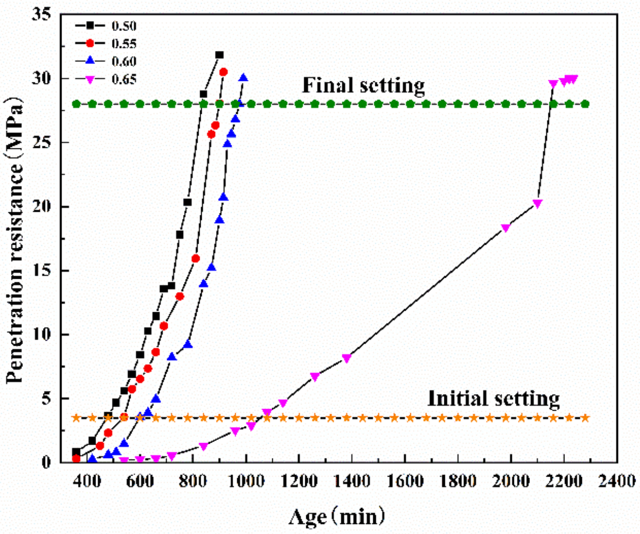

Figure 3. Setting times of RCGC slurry samples with four different water-binder ratios (0.50,0.55,0.60, and 0.65).

3.3. Electrochemical impedance characteristics

Figures 4(a)-(f) are Nyquist plots of different curing ages, with both the real part (*Z*′) and imaginary part (*Z*″) of the impedance considered. In Fig. 4, the electrochemical impedance spectra of RCGC materials of different ages are mainly composed of semi-circular capacitive reactance arcs. The semi-circular capacitive reactance arc indicates that a gel substance had been generated by electrochemical reaction inside the RCGC sample, and a corresponding gel system was formed 30[32].

As shown in Fig. 5, the RCGC material with a water-binder ratio of 0.50 as an example, the diameter of the semi-circular capacitive reactance arc increases with time during the entire testing process. This is consistent with the findings of Fang et al. [33]. The increased semi-circular diameter means that the volume resistance of the RCGC sample also increases [34]; as the test progresses, the capacitive reactance arc gradually shifts to the right.

From the Nyquist plots of RCGC specimens with different water-to-binder ratios and coagulation hardening for specimens aged for 1 d, as illustrated in Fig. 4(a), the diameter of the semi-circular capacitive arc is smaller, which indicates that electrochemical reaction in the RCGC material is not particularly obvious. This is because the existence of different ion conduction paths in the geopolymer solution, mainly including the following three: the geopolymer gel, the pore solution inside the sample, and the alternating transfer between the geopolymer gel and the pore solution. After the curing age reaches 1 d, the polymerization reaction inside the RCGC sample has not yet been completed, and the amount of the generated geopolymer gel material is very small, which cannot provide sufficient conductive paths, so that the internal electrochemical reaction is not very significant. At 3 d of coagulation and hardening, as shown in Fig. 4(b), the polymerization reaction is completed compared with 1 d, and a large amount of geopolymer gel substances can be generated; these gel substances accumulate inside the test block to form sufficient conductive paths, facilitating the electrochemical reaction as normal, and a connected pore structure is formed within the RCGC sample. As shown in Figs. 4(c) and (d), the diameter of the semi-circular capacitive arc increases greatly and shifts significantly to the right. When the curing age reaches 14-28 d, as shown in Figs. 4(d) and (e), the rate of change in the diameter of the semi-circular capacitive reactance arc in the Nyquist diagram decreases. This is because the coagulation and hardening reaction is in a stable state, the polymerization reaction inside the RCGC has been completed, and the complete pore structure has been formed inside the RCGC material [35]. In addition, as the water-binder ratio increases, the diameter of the semi-circular capacitive reactance arc gradually decreases, and the impedance curve shifts to the left as a whole. This is because with the increase of the water-binder ratio, the free water inside the sample increases, at the same time, the degree of reaction of the geopolymer in the system gradually decreases, the generated geopolymer gel material gradually decreases, and the electrochemical reaction weakens accordingly.

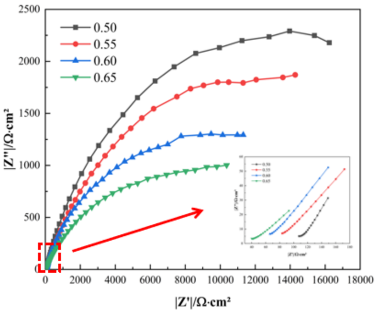

（a）1 d

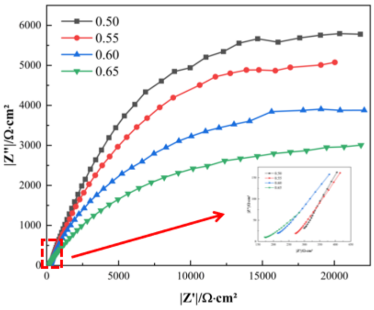

（b）3 d

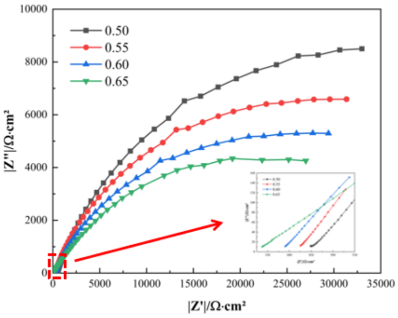

（c）7 d

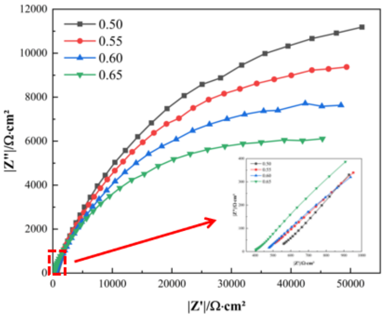

（d）14 d

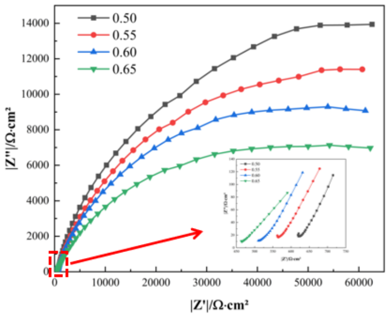

（e）21 d

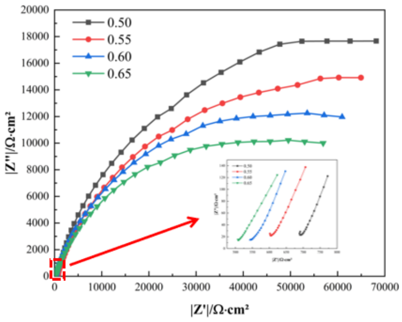

（f）28 d

Figure 4. The Nyquist plots of the EIS diagram for RCGC samples with different water-binder ratios (0.50,0.55,0.60, and 0.65) for 1-28 d.

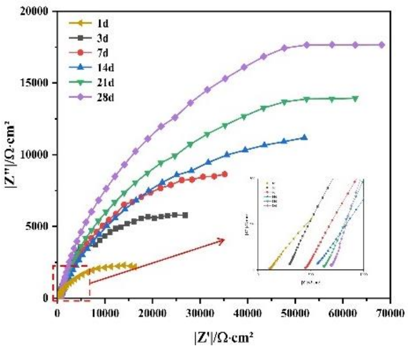

Figure 5. The Nyquist plots of RCGC samples with a water-binder ratio of 0.50 for 1-28 d.

To obtain a large amount of EIS-related information, a suitable equivalent circuit is generally used for correlation and regression analysis. Usually, the equivalent circuit model can be established by using capacitors, resistors, and other components in series or parallel [36-37]. On this basis, a constant phase element (CPE) is employed to avoid the diffusion effect. As shown in Fig. 6, the circuit model uses $R_s(\mathrm{CPE}(R_{ct}C))$, where R_s represents the resistance of the electrolyte solution, and CPE denotes the electric double layer capacitance, where CPE = $K(\mathrm{j}\omega)^{-q}$, q represents the degree of flattening of the capacitive arc, the fractal dimension $d_s = 3 - q$ [38], which can quantitatively describe the compactness of the microstructure, R_{ct} is the resistance caused by charge transfer, and C is the pure resistance capacitance. The total impedance of the equivalent circuit model is:

$$Z = R_S + \cfrac{1}{j\omega C_d + \cfrac{1}{R_{ct} + \cfrac{1}{\omega C}}}$$

By using Z-view and ZSimDemo3.30d software to study the correlation fitting of the equivalent circuit, the following parameters can be obtained: the specific values of R_s, R_{ct}, q, and d_s. These parameters are closely related to the mechanical properties and internal microstructure characteristics of

RCGC materials, which are the focus of research into the solidification and hardening of RCGC materials.

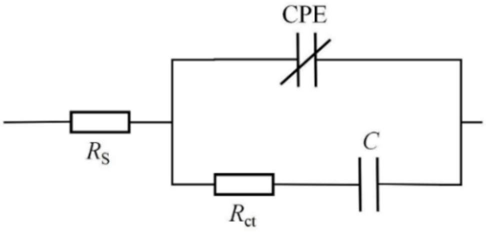

Figure 6. Equivalent circuit diagram of the RCGC sample.

The impedance parameter R_s values of RCGC materials with four water-binder ratios are displayed in the Table 2 and Fig. 7. The R_s value is the total concentration and total porosity of the identified ions [39-40]. Theoretically, with the progress of coagulation and hardening, the total ion concentration in the pore solution inside the system will increase significantly, and the corresponding R_s value should be greatly reduced. However, Fig. 7 implies that the R_s value increases with the increases of the setting and hardening time, and the increase rate of the parameter value will gradually decrease as setting and hardening progresses. With the increase of age, the internal geological structure and reaction of the system reach a certain level, generally 1 to 3 d, the total ion concentration in the pore solution of the RCGC sample will gradually stabilize, but due to the continuous generation of geopolymer condensation, glue will occupy a part of the pores [41-42], resulting in a continuous decrease in the porosity. The increase rate of the parameter value decreases because there is less space available for the cement hydration products to fill with the hydration process, and the rate of decrease in the porosity decreases. A similar phenomenon can be found in the study by Niu et al. [35]. In addition, the impedance parameter R_s of the RCGC material is also shown to increase greatly with the decrease of the water-binder ratio.

Table 2. The values of impedance parameter Rs for 1-28d and four water-binder ratios.

Water-binder ratio	Impedance parameter Rs/(Ω·cm^2)					
	1d	3d	7d	14d	21d	28d
0.50	107	299	451	2560	623	681
0.55	83	271	425	512	562	601
0.60	65	213	390	478	510	543
0.65	39	172	337	403	463	507

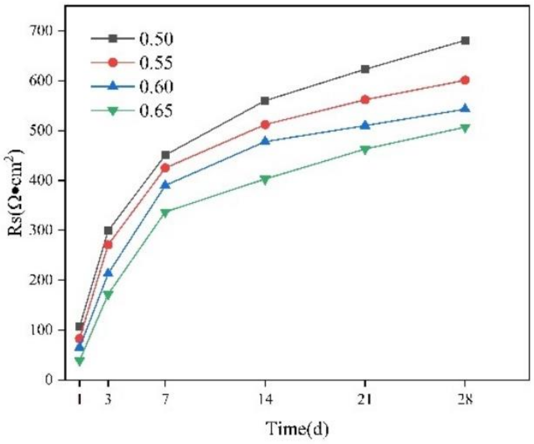

Figure 7. The values of impedance parameter Rs for 1-28 d and four water-binder ratios.

The diameter of the semi-circular capacitive reactance arc in the Nyquist diagram is the impedance parameter (R_{ct}) [43]. The resistance parameter R_{ct} essentially reflects the extent of densification of the RCGC microstructure. The values of the impedance parameter R_{ct1} of RCGC materials with four water-binder ratios are preasented in Table 3 and Fig. 8. After 1 d of coagulation and hardening, due to the low degree of geopolymerization, the value of the impedance parameter R_{ct} is also small, which matches the results in the literature [42]. The value of the impedance parameter R_{ct} increases rapidly with the curing age, because the space material inside the RCGC is rapidly filled with the gel product, which leads to the densification of the pores and microstructure. After 7 d to 14 d of coagulation and hardening, the resistance parameter R_{ct} increases slowly, because the space that the hardened product can fill is greatly reduced. Therefore, throughout the process of coagulation and hardening, the impedance parameter R_{ct} will increase continuously, and the internal microstructure of the RCGC system will become more dense. This is consistent with literature results [33]. In addition, with the decrease of the water-binder ratio, the impedance parameter R_{ct} will continue to increase, showing the same trend as the impedance parameter R_s. There are two main reasons for these R_s and R_{ct} values to increase gradually with decreasing water-binder ratio. (1) The decrease of the water-binder ratio will increase the total ion concentration in the pore solution[30]. (2) The decrease of the water-binder ratio will accelerate geopolymerization and increase the amount of gel material generated, thereby reducing the porosity. This results in an increase in the compactness of the microstructure of the RCGC material, impairing ion transport in the pore solution.

Table 3. The values of impedance parameter R_{ct} for 1-28 d and four water-binder ratios.

Water-binder ratio	Impedance parameter R_{ct} / (Ω·cm^2)					
	1d	3d	7d	14d	21d	28d
0.50	2.0×10^4	3.8×10^4	4.9×10^4	5.8×10^4	6.6×10^4	7.2×10^4
0.55	1.7×10^4	3.2×10^4	4.2×10^4	5.2×10^4	6.0×10^4	6.5×10^4
0.60	1.4×10^4	2.9×10^4	3.8×10^4	4.7×10^4	5.6×10^4	6.1×10^4
0.65	1.2×10^4	2.5×10^4	3.5×10^4	4.4×10^4	5.4×10^4	5.8×10^4

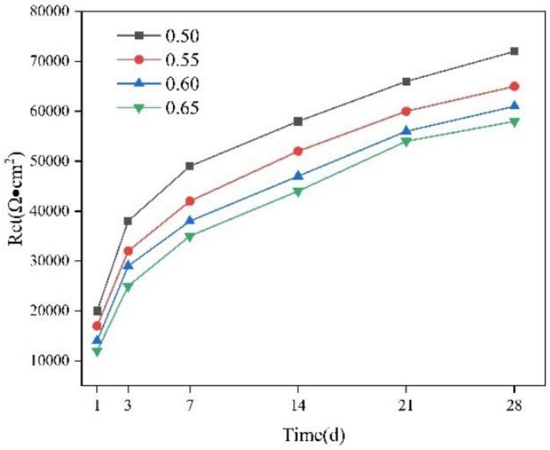

Figure 8. The values of impedance parameter R_{ct} for 1-28 d and four water-binder ratios.

The contents of constant phase index q and fractal dimension d_s of RCGC materials with different water-binder ratios are shown in Table 4. The fractal dimension d_s reflects the compactness of the microstructure of the RCGC material. The smaller the value of ds, the smaller the average pore size and the median pore size, and the denser the microstructure of the RCGC material. The constant phase index q reflects the flatness of the high-frequency semicircle. As the setting and hardening time increases, the value of the parameter q increases, and the value of the fractal dimension d_s decreases accordingly. This indicates that during the coagulation and hardening process, the number of small pores increases, the number of large pores decreases, the pore size distribution is optimized, and the microstructure develops gradually therewith. This is consistent with other published results [42]. After 28 d of hydration, the d_s values of RCGC materials with different water-to-binder ratios are close to 2. This matches the literature results [35]. The value of q increases with the increase of the water-binder ratio in the same setting and hardening period, but the fractal dimension d_s decreases gradually. This phenomenon is due to the fact CMK will undergo geopolymerization with RM and the alkaline activator to generate more geopolymerization products, fill part of the pores, which thereby reduces the porosity, decreases the size of the larger pores, and increase the number of those smaller pores in the RCGC, changing their distribution within the material system.

Table 4. The values of the constant phase index(q) and fractal dimension(d_s) for 1-28 d and four water -binder ratios.

Curing age (d)	0.50		0.55		0.60		0.65	
	q	ds	q	ds	q	ds	q	ds
1	0.768	2.232	0.762	2.238	0.759	2.241	0.754	2.246
3	0.784	2.216	0.777	2.223	0.773	2.227	0.760	2.24
7	0.802	2.198	0.795	2.205	0.789	2.211	0.786	2.214
14	0.809	2.191	0.801	2.199	0.797	2.203	0.793	2.207
21	0.813	2.187	0.806	2.194	0.802	2.198	0.796	2.204
28	0.816	2.184	0.809	2.191	0.806	2.194	0.801	2.199

3.4. Compressive strength

The compressive strength of the RCGC samples (1-28 d) are shown in Fig. 9. As expected, the compressive strength of the RCGC samples increases with the curing age, but it was found that there are significant differences in the trend of compressive strength with different water-binder ratios. During the whole curing process, the strength of the RCGC samples decrease significantly with the increase of the water-binder ratio. The 28-day compressive strength of RCGC samples with water-binder ratios of 0.55, 0.60, and 0.65 decrease by 12.1%, 22.3%, and 34.4%, relative to the samples with water-binder ratio of 0.50. A similar phenomenon was found in the study by Aliabdo et al. [30]. Among them, the compressive strength of the RCGC sample with a water-binder ratio of 0.50 can reach more than 80% of the 28-day compressive strength in 7 days, indicating that the material has the characteristics of early and rapid hardening.

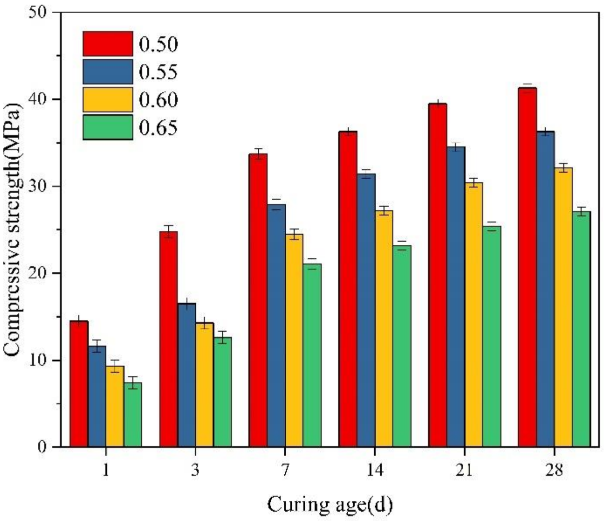

Figure 9. Compressive strength of RMGC samples with different water-binder ratios for 1-28 d.

The dissolution and geopolymerization reaction process of red mud and coal metakaolin in a highly alkaline environment can be as shown in the following equation [44]:

(a) $(\text{Si-Al solid}) + \text{OH}^- \rightarrow [\text{Al(OH)}_4]^- + [\text{SiO(OH)}_3]^- + [\text{SiO}_2(\text{OH})_2]^{2-} + [\text{SiO}_3(\text{OH})_2]^{3-}$

(b) $[\text{SiO(OH)}_3]^- + [\text{Al(OH)}_4]^- \rightarrow [(\text{OH})_2\text{OSi-O-Al(OH)}_3]^{2-} + \text{H}_2\text{O}$

(c) $[\text{SiO(OH)}_3]^- + [\text{SiO(OH)}_3]^- \rightarrow [(\text{OH})_2\text{OSi-O-Si(OH)}_2]^{2-} + \text{H}_2\text{O}$

(d) $[\text{SiO(OH)}_3]^- + [\text{SiO}_2(\text{OH})_2]^{2-} \rightarrow [(\text{OH})_2\text{OSi-O-SiO}_2(\text{OH})_2]^{3-} + \text{H}_2\text{O}$

(e) $[\text{SiO(OH)}_3]^- + [\text{SiO}_3(\text{OH})]^{3-} \rightarrow [(\text{OH})_2\text{OSi-O-SiO}_3]^{4-} + \text{H}_2\text{O}$

(f) $2\ \text{silicate dimers} + 2\ \text{silicate cyclic} \rightarrow \text{cyclic trimer} + \text{linear trimer} + 2\text{OH}^-$

Formula (a) shows that the silicon and aluminum components in the raw materials (RM and CMK) will dissolve into Si and Al active monomers and react with OH^- in a highly alkaline environment to obtain four kinds of ions. Formulae (b) to (f) show that these ions will continue to diffuse in the pore solution and further synthesize into dimer and trimer aluminosilicate ions: finally, these aluminosilicate ions will aggregate to form a three-dimensional network of geopolymer gels, however, a certain amount of water will be released during the polymerization reaction. With the decrease of the water-binder ratio of the RCGC samples, the free water content in the solution decreases significantly. First, the increased free water will slow the forward reaction of equations (b) to (f), breaking the balance of the original polymerization process, and slowing the entire geopolymerization process. Secondly, some free water will remain between the particles and in the macropores and will be gradually evaporated as the curing process progresses, and the space occupied by the evaporated water will leave a large number of circular cavities in the microstructure. Both these possibilities will adversely affect the strength of the RCGC samples. The results obtained in this study match other studies [30,45].

The impedance parameters R_s and R_{ct} can reflect the changes in the microstructure of RCGC materials (with good sensitivity); these are closely related to the compressive strength of RCGC materials. Therefore, in this paper, the impedance parameters R_s and R_{ct} are fitted linearly with the compressive strength. As shown in Figs. 10 and 11, a linear function ($Y = AX + B$) is used for linear regression, and the correlation coefficient R^2 in the fitting results is greater than 0.90, indicating the good correlation between the impedance parameters R_s and R_{ct} and the compressive strength [33,35,46]. Moreover, the slope of the curve gradually increases with the increase of the water-binder ratio.In conclusion, EIS can be used as a new non-destructive testing method for geopolymer concrete, and the compressive strength development of RCGC materials within 28 days of curing can be predicted by EIS.

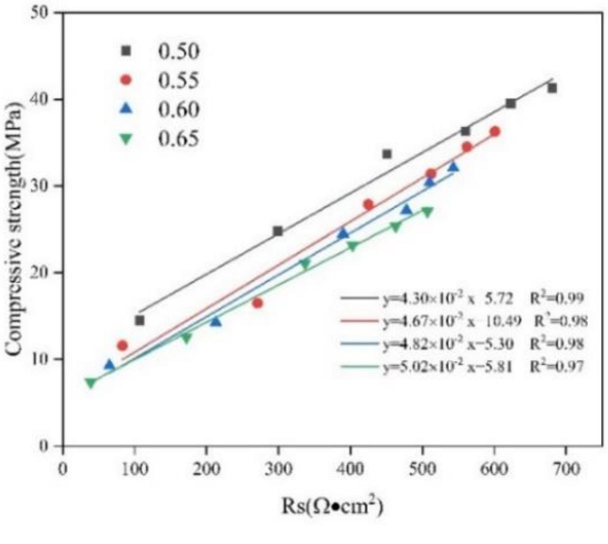

Figure 10. The correlation between the compressive strength and the impedance parameter Rs for the RCGC samples.

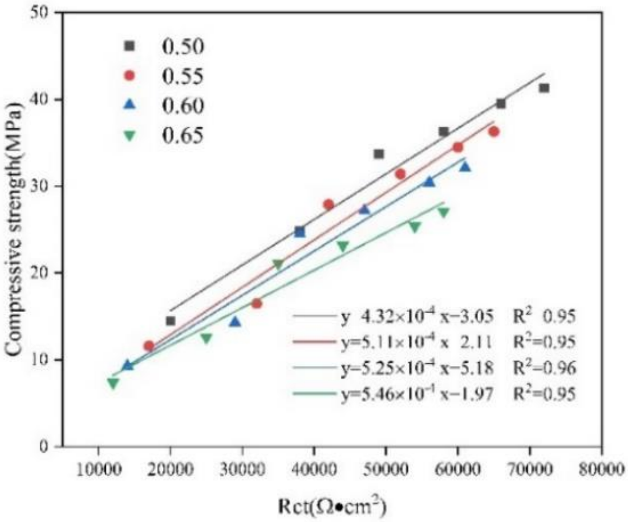

Figure 11. The correlation between the compressive strength and the impedance parameter *R*ct for the RCGC samples.

In terms of workability, when the water-binder ratio is less than 0.50, the material takes a lot of time during the stirring process, and it is difficult to shape. When the water-binder ratio is greater than 0.50, the workability of the material is getting better and better. The setting time increases significantly with the increase of the water-binder ratio, and the compressive strength decreases significantly with the increase of the water-binder ratio. Based on the above research, the RCGC sample with a water-to-binder ratio of 0.50 was selected to conduct a more detailed exploration of the mechanism of the coagulation and hardening of the material. The following RCGC samples with a water-binder ratio of 0.50 are abbreviated as GC0.5.

3.5. NMR analysis

NMR technology utilizes the relaxation characteristics of water molecules in the material pores under the action of a magnetic field and can collect the distribution of the transverse relaxation time T_2 without damaging the material, so that the change information of the pore structure can be quantitatively obtained [47]. The distribution map of T_2 at different ages is shown in Fig. 12. The longer the transverse relaxation time T_2, the larger the number of pores in the material, and vice versa. Fig. 12 indicates that the distribution pattern of T_2 is composed of one main peak and two secondary peaks. The area and height of the main peak are much larger than those of the secondary peak. The main peak is between 0.05 and 3 ms and the secondary peak is between 10^1 –10^4 ms. This shows that the main peak is related to the presence of small pores, and the secondary peak arises from the presence of those larger pores. Similar phenomena can be found in the study by She et al. [48]. With the increase of age, the area and height of the main peak and the two secondary peaks decrease, indicating that the number of pores in the material decreases with the progress of the internal reaction of the GC0.5 sample. Compared with the total porosity on 1 d, the total porosity of the 28-day GC0.5 samples decreased by 14.68%.

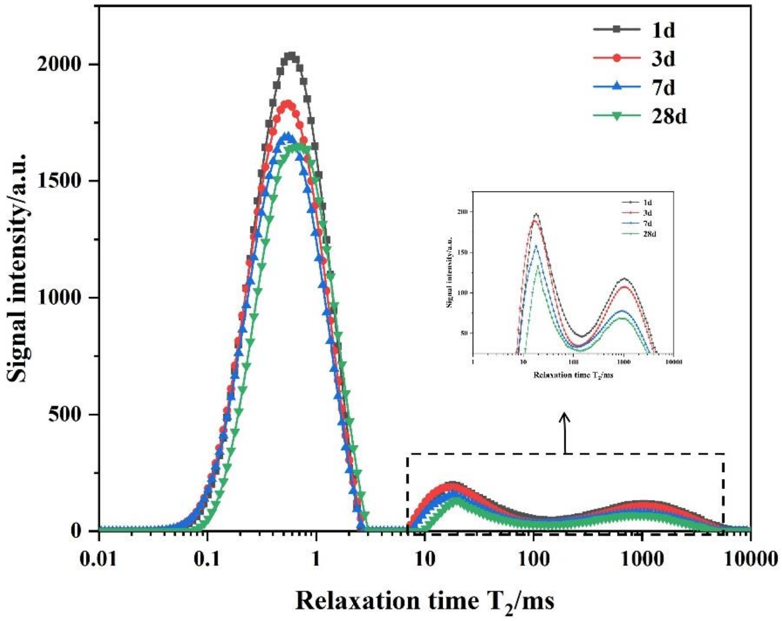

Figure 12. T_2 distribution of GC0.5 samples at different curing ages(1d, 3d, 7d, and 28d).

According to Yang *et al.* [49], the pore size classification is also a factor that affects the compressive strength. Those with a pore aperture size of less than 0.02 μm are deemed harmless, those with a pore aperture size between 0.02 and 0.05 μm are deemed less harmful, and those with a pore aperture size greater than 0.05 μm are deemed harmful. Fig. 8 shows the pore size distribution of geopolymer concrete.

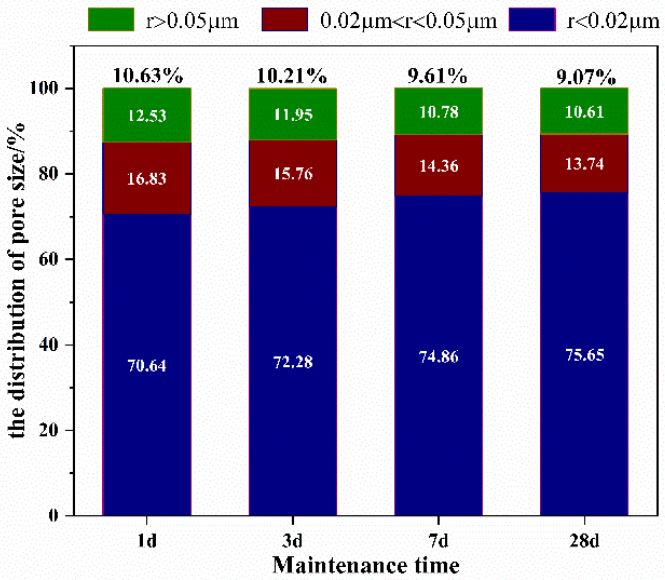

Figure 13. Histogram of the pore gradation distribution of GC0.5 samples at different curing ages(1d, 3d, 7d, and 28d).

During the first 28 days of curing, over time, the proportion of harmless pores in the total continued to increase (the total increase over 28 days is 8.62%); harmful pores showed a decreasing trend (decreasing by 30.34% and 27.75% in 28 days). Since the internal polymerization reaction of the GC0.5 sample will continue, the hardened product generated will fill a part of the pores of the large pore size and harmful pores, and the large pore size and harmful pores will gradually evolve into smaller, less harmful or harmless pores. As the structure becomes more fully developed, the compressive strength of the GC0.5 samples increases: this is consistent with the findings obtained by EIS. The results of this study match other study [50].

3.6. XRD analysis

Fig. 14 shows XRD spectra of the 1, 7, and 28-d GC0.5 samples. During the 28-d curing period, the crystalline phase strength of cannonite and katoite is almost unchanged. In the Fig.14, the diffraction peak intensity of quartz crystals decreases with age within 28 d, indicating that a small amount of quartz crystals had dissolved in the solution in an alkaline environment [51]. The crystalline phase strength of albite and microcline decreased significantly from 1 to 28 d. The albite and microcline will dissolve in the solution in a highly alkaline environment, and the dissolved product is conducive to further polymerization to generate a geopolymer gel substance. Under alkaline conditions, the reaction of albite and microcline are shown below:

Albite ($NaAlSi_3O_8$):

$$\mathrm{NaAlSi_3O_8 + 2H_2O + 6OH^- \Leftrightarrow Al(OH)_4^- + 3H_2SiO_4^{2-} + Na^+} \qquad (1)$$

Microcline ($KAlSi_3O_8$):

$$\mathrm{KAlSi_3O_8 + 2H_2O + 6OH^- \Leftrightarrow Al(OH)_4^- + 3H_2SiO_4^{2-} + K^+} \qquad (2)$$

This is consistent with other observations of geopolymer systems [52-53]. The formation of zeolite mineral minerals is observed in the Fig. 14. Zeolite minerals are formed by the reaction of OH^- ions in the pore solution with the silica-alumina components in the GC0.5 samples [23].

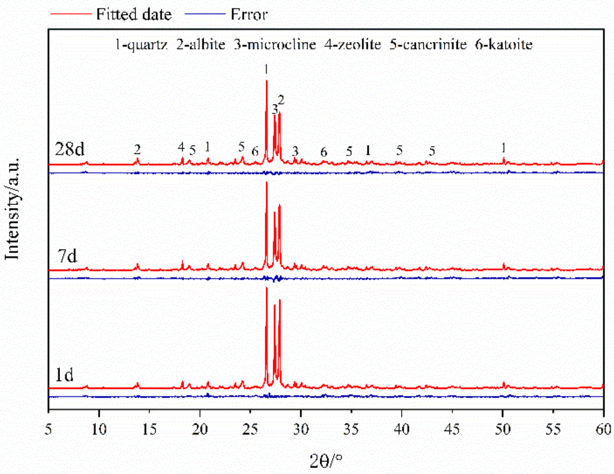

Figure 14. XRD spectra of GC0.50 samples at different curing ages (1d, 7d, and 28d).

Since the GC0.5 sample is an amorphous aluminosilicate, as can be seen from Fig. 14, a slightly raised diffraction peak envelope appears in the interval $25° \leq 2\theta \leq 30°$, and the effect persists with age, indicating the formation of a geopolymer gel phase [54]. The crystallinity at three different ages was calculated through JADE6 software analysis, using the following equation [55]:

$$C = \frac{S_1}{S_2} \times 100\%$$

C: degree of crystallinity;
S_1: sum of the areas under the peaks;
S_2: sum of the XRD peaks and areas under peaks in a specific region.

The crystallinity of the samples at three different ages (1, 7, and 28-d) was determined to be 94.56%, 92.32%, and 89.63% respectively. This indicates that the amount of amorphous geopolymer gel formation increases gradually within the 28 d curing period.

3.7. SEM-EDS analysis

Fig. 15(a)-(d) are SEM images of geopolymer concrete hardening for 1, 3, 7, and 28-d under standard curing conditions. From Fig. 15(a), after curing for 1 day, a small amount of gel material is formed, and the gel material is attached to some powder particles that have not yet reacted; there are many pores in the GC0.5 sample system at that time, and its structure is relatively loose. At 1 d, the rate of gel formation is slow so no stable three-dimensional network structure can be formed at this juncture. After curing for 3 d, the number of unreacted particles is greatly reduced, and the amounts of fibrous products and flocculent aluminosilicate gels formed significantly increase. The generation of larger pores in the 3-d samples may have been caused by external forces during the preparation of the samples. After curing for 7 d, many foil-like products will be formed, and these foil-like products will be superimposed on each other, becoming tightly connected, and the density of the structure will be significantly increased. After curing for 28 d, the surface of the sample is smooth and flat, and the compressive strength of the sample is maximized at that time. The mechanical strength of the geopolymer was related to their microstructure with the less porous samples being the strongest. Similar findings were also found in the study by FUA et al. [56].

Fig. 16(a)-(d) show the elemental distribution diagrams of GC0.5 samples at different ages (1, 3, 7, and 28-d). From Fig. 16(a), it can be observed that the amount of Na, Al, Si, and Ca is very small, indicating that the amount of the elements dissolved in the raw material is very small, and there will be a large amount of unreacted raw material powder particles at that time. This is consistent with the literature results [23].Compared with Fig. 11(a), the number of elements shown in Fig. 16(b) is significantly increased, and it can be observed that the space-filling Ca element rarely appears in the presence of Si and Al, indicating that these products are geopolymer gel substances [57]. From the element distributions in (b) and (c), it can be speculated that this flake product may be $NaCaHSiO_4$ (sodium calcium silicate). The elements shown in Fig. 1(d) are present in large quantities and are uniformly distributed, indicating that the products generated by the reaction are uniformly distributed, and the mechanical strength of the GC0.5 sample material is maximized at this time.

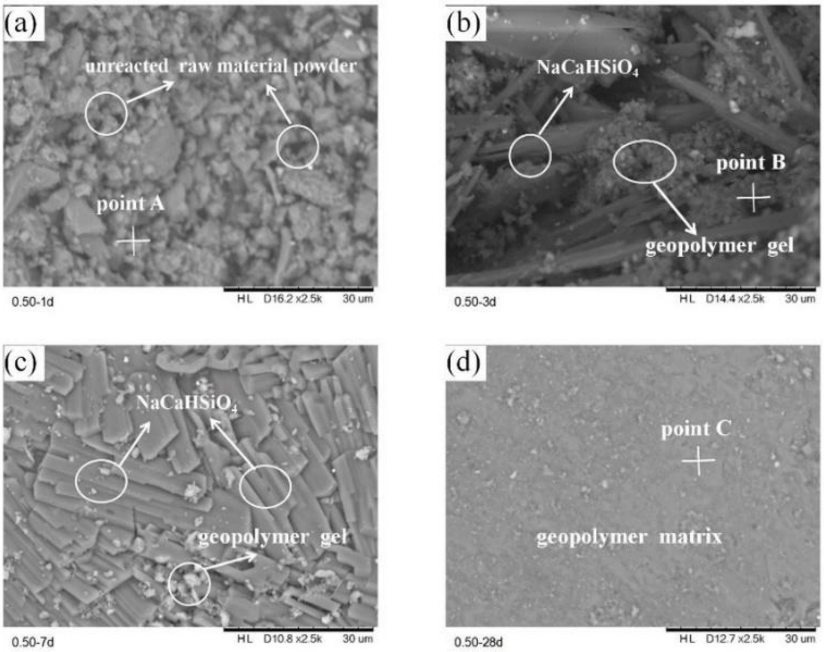

Figure 15. SEM images of GC0.5 samples at different curing ages (1d, 3d, 7d, and 28d).

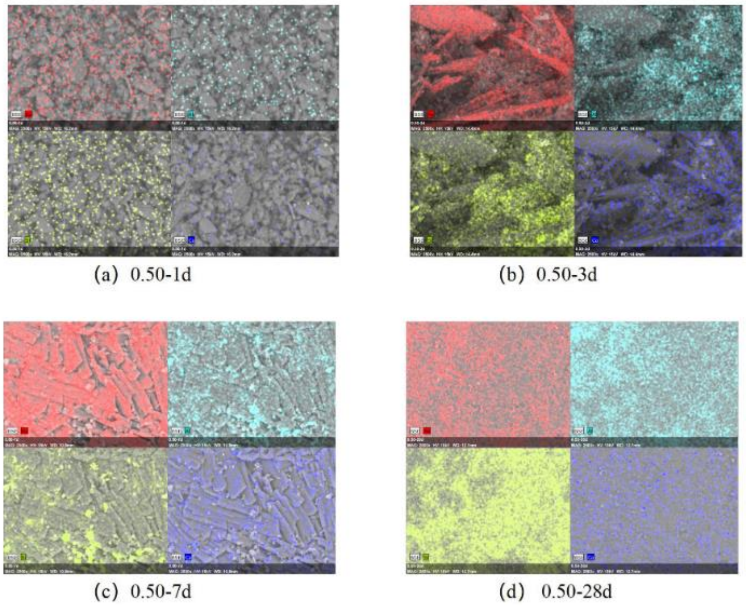

Figure 16. Elemental distribution map of GC0.5 samples at different curing ages (red: Na, light blue: Al, yellow: Si, dark blue: Ca).

Fig. 17(a)-(c) are the EDS patterns of the three points marked in the SEM image of the GC0.5 sample. It has been reported that the silica-alumina ratio can be used to characterize the degree of polymerization of the internal reaction of the geopolymer and the compactness of the microstructure in the gel material [58]. Table 5 lists the amounts of each element at three points: the result of calculation the silicon-aluminum ratio at points A, B, and C gradually increase, indicating that during the 28-day curing period, the geopolymerization reaction generates more gel substances, which is consistent with the results obtained by XRD and explain why the compressive strength of the material is enhancing.

Table 5. Contents of different elements of areas A, B, and C as detected by EDS.

Point	Element (atomic ratios, %)						Molar ratios Si/Al
	Ca	O	Na	Al	Si	Au	
A	2.07	68.84	9.72	8.34	10.01	1.02	1.20
B	3.11	62.55	11.01	9.89	12.36	1.13	1.25
C	5.34	57.73	8.92	10.67	14.22	3.11	1.33

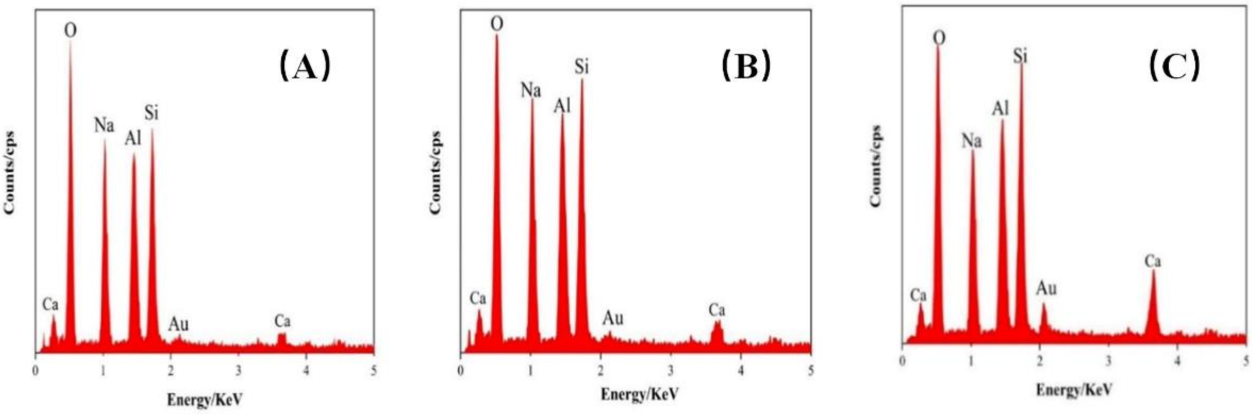

Figure 17. EDS diagrams of GC0.5 sample in three points(A, B, and C).

4. CONCLUSIONS

In this study, the impedance parameters (R_s and R_{ct}) and fractal dimension of RCGC materials were analyzed by electrochemical impedance spectroscopy and equivalent circuit fitting analysis. Taking a water-binder ratio of 0.50 as an example, the phase composition, pore change, and microstructure of RCGC materials were investigated using XRD, NMR, and SEM-EDS. The following conclusions were obtained:

(1) The variation of the water-binder ratio changes the coagulation and hardening process of RCGC materials. The increase of the water-binder ratio will significantly prolong the setting time of the RCGC material and improve the working performance of the RCGC material accordingly.

(2) The Nyquist diagram of the RCGC material is mainly composed of semi-circular capacitive reactance arcs, the diameter of which decreases with the increase of the water-to-binder ratio, and the capacitive reactance arcs gradually shift to the left. In addition, the diameters of the semi-circular capacitive reactance arcs of the Nyquist plots at different curing ages increase with time, and the capacitive reactance arcs gradually shift to the right. The impedance parameters R_s and R_{ct} of the RCGC material decrease with the increase of the water-binder ratio and increase with the progress of the coagulation and hardening process, and the fractal dimension d_s gradually increases with the increase in the water-binder ratio. This suggests that the reduction of the water-binder ratio reduces the overall porosity of the RCGC material and densifies the microstructure thereof.

(3) The compressive strength shows a similar increasing trend to the impedance parameters R_s and R_{ct}. The impedance parameters R_s and R_{ct} are significantly correlated with the compressive strength, and the relationship is quasi-linear with all correlation coefficients exceeding 0.90. Non-destructive monitoring of the compressive strength of RCGC is thus deemed to be feasible.

(4) XRD and EDS analysis results show that with the increase of curing age, the degree of polymerization increases significantly, and the amount of aluminosilicate polymer formed increases. The results of scanning electron microscopy and nuclear magnetic resonance analysis show that the amorphous geopolymer gel formed continuously in RCGC fill some of the pores, and the large pore size pores gradually evolve into small pore size pores, which optimized the pore structure characteristics of RCGC. The findings of the study correspond to the electrochemical studies and explain the changes in the impedance parameters R_s and R_{ct}.

ACKNOWLEDGEMENTS

The present work is supported by the National Natural Science Foundation of China (No: 51879180,41807256), the Natural Science Foundation of Shanxi Province (20210302123139, 20210302124662, 20210302424613).

References

1. A. Gholampour and T. Ozbakkaloglu, *J. Cleaner Prod.*, 162 (2017) 1407.
2. A. Mehta and R. Siddique, *J. Cleaner Prod.*, 205 (2018) 49.
3. A. Hasanbeigi, C. Menke and L. Price, *J. Cleaner Prod.*, 18 (15) (2010)1509.
4. D. N. Huntzinger and T. D. Eatmon, *J. Cleaner Prod.*, 17 (7) (2009) 668.
5. L. Assi, K. Carter, E. Deaver, R. Anay and P. Ziehl, *J. Cleaner Prod.*, 198 (2018) 1641.
6. R. C. Kaze, L. M. B. à Moungam, M. L. Fonkwe Djouka, A Nana, E Kamseu, U. F. Chinje Melo and C. Leonelli, *Appl. Clay Sci.*, 138 (2017) 48.
7. B. Singh, G. Ishwarya, M. Gupta and S. K. Bhattacharyya, *Constr. Build. Mater.*, 85 (2015) 78.
8. S. E. Wallah, D. M. J. Sumajouw, B. V. Rangan and D. Hardjito, *ACI Mater. J.*, 101 (6) (2004) 467.
9. D. M. J. Sumajouw, D. Hardjito, S. E. Wallah and B. V. Rangan, J. Mater. Sci. 42 (9) (2006) 3124.
10. W. Hajjaji, S. Andrejkovičová, C. Zanelli, M. Alshaaer, M. Dondi, J.A. Labrincha and F. Rocha, *Mater. Des.*, 52 (2013) 648,
11. A. Nazari, A. Bagheri and S. Riahi, *Mater. Sci. Eng., A.*, 528 (24) (2011) 7395.
12. F. Pacheco-Torgal, J. Castro-Gomes and S. Jalali, *Constr. Build. Mater.*, 22 (7) (2008) 1315.
13. P. Duxson, S. W. Mallicoat, G. C. Lukey, W. M. Kriven and J. S. van Deventer, *Colloids Surf., A.*, 292 (1) (2007) 8.

14. F. Pelisser, E. L. Guerrino, M. Menger, M. D. Michel and J. A. Labrincha, *Constr. Build. Mater.*, 49 (2013) 547.
15. J. E. Oh, P. J. M. Monteiro, S. S. Jun, S. Choi and S. M. Clark, *Cem. Concr. Res.*, 40 (2) (2010) 189.
16. S. Aydın and B. Baradan, *Mater. Des.*, 35 (2012) 374.
17. J. He, Y. Jie, J. Zhang, Y. Yu and G. Zhang, *Cem. Concr. Compos.*, 37 (1) (2013) 108.
18. Z. Sun, Q. Tang, B. S. Xakalashe, X. Fan, M. Gan, X. Chen, Z. Ji, X. Huang and B. Friedrich, *Constr. Build. Mater.*, 321 (2022) 125564.
19. S. K. U. Rehman, L. Imtiaz, F. Aslam, M. K. Khan, M. Haseeb, M. F. Javed, R. Alyousef and H. Alabduljabbar, *Mater.*, 13 (15) (2020) E3437.
20. L. Wang, X. Li, Y. Cheng and X. Bai, *Constr. Build. Mater.*, 166 (2018) 592.
21. G. Ascensao, M. P. Seabra, J. B. Aguiar and J. A. Labrincha, *J. Cleaner Prod.*, 148 (2017) 23.
22. F. Lyu, Y. Hu, L. Wang and W. Sun, *J. Hazard. Mater.*, 403 (2021) 123671,.
23. J. Liu, X. Li, Y. Lu and X. Bai, *Constr. Build. Mater.*, 263 (2020) 120653.
24. S. Y. Pu, Z. D. Zhu, W. L. Song, W. W. Huo and J. Zhang, *Constr. Build. Mater.*, 299 (2021) 123947.
25. S. Zhou, Z. Yang, R. Zhang and F. Li, Preparation, *J. Cleaner Prod.*, 312 (2021) 127822.
26. D. Madej and A. Kruk, *Constr. Build. Mater.*, 206 (2019) 307.
27. S. W. Niu, , F. N. Sun, R. Z. Xie, B.He, F. L. Ma, X. A. Guo A. A. Fattah, X. Y. Wang and P. J. Han, *Int. J. Electrochem. Sci.*, 15 (2020) 12264.
28. Chinese Standard, Standard for Test Methods of Mechanical Properties of Ordinary Concrete, GB/T 50080–2016, China Construction Industry Press, Beijing, China, 2017.
29. Chinese Standard, Standard for Test Method of Performance on Building Mortar, GB/T 50081-2019, China Construction Industry Press, Beijing, China, 2019.
30. A. A. Aliabdo, M. Abd Elmoaty and H. A. Salem, *Constr. Build. Mater.*, 121 (2016) 694.
31. H. T. Adnan, K. Abigail and T. Robert J. *Constr. Build. Mater.*, 352 (2022) 128979.
32. M. Cabezaa, P. Merino, A. Mirandab, X.R. Nóvoaa and I. Sanchez, *Cem. Concr. Res.* 32 (6) (2002) 881.
33. Y. Fang, H. B. Li, Z. H. Wang, K.D. Zhang, P. Cui and B. Q. Dong, *IOP Conf. Series: Earth and Environmental Science*, 300 (5) (2019).
34. S. Zeng and J. Wang, *Constr. Build. Mater.*, 121 (2016) 386.
35. S. W. Niu, P. J. Han, F. N. Sun, R. Z. Xie, B.He, F. L. Ma, X. A. Guo and A. A. Fattah, *Int. J. Electrochem. Sci.*, 15 (2020) 9428.
36. D. Ravikumar and N. Neithalath, *Cem. Concr. Compos.*, 44 (2013) 58.
37. J. M. Cai, J. L. Pan, X. P. Li, J. W. Tian and J. B. Li, *Constr. Build. Mater.*, 234 (2020) 117868.
38. W. J. McCarter, *Adv. Cem. Res.*, 6 (24) (1994) 147.
39. H. Ma and Z. Li, *Comput. Concr.,* 11 (4) (2013) 317.
40. C. Çetin, S.T. Erdogan and M. Tokyay, *Cem. Concr. Comp.*, 67 (2015) 39.
41. I. Janotka, F. Puertas and M. Palacios, Constr. Build. Mater., 24 (5) (2010) 791.
42. F.J. Jiang, J.X. Gong and W. Zhang, *J.Xi'an Univ. of Arch.& Tech.*, 48 (4) (2016) 493.
43. M.L. Shi, *Impedance Spectroscopy of Concrete, China Railway Press*, (2003) Beijing, China.
44. H. Xu and J. S. J. Van Deventer, *Int. J. Miner. Process.*, 59 (2000) 247.
45. A. Sathonsaowaphak, P. Chindaprasirt and K. Pimraksa, *J. Hazard. Mater.*, 168 (1) (2009) 44.
46. T. T. Guo, T. Wu, L. M. Gao, B. He, F. L. Ma, Z. F. Huang and X. H. Bai, *Constr. Build. Mater.*, 303 (2021) 124523.
47. P. Pipilikaki and M. Beazi-Katsioti, *Constr. Build. Mater.*, 23 (5) (2009) 1966.
48. A. M. She, K. Ma, G. Liao, W. Yao and J. Q. Zuo, *Constr. Build. Mater.*, 304 (2021) 124631.
49. R. H. Yang, B. Y. Liu and Z. W. Wu, *Cem. Concr Res.*, 20 (1990) 385.
50. J. H. Chen, Y. L. Li, H. Zhou, Y. Li and H.Y. Guo, *JOM.*, 74 (5) (2022) 1047.
51. J. Temuujin, A. van Riessen and K. J. D. MacKenzie, *Constr. Build. Mater.*, 24 (10) (2010)1906.
52. W. K. W. Lee and J. S. J. van Deventer, *Cem. Concr Res.*, 37 (6) (2007) 844.
53. S. Chuah, W. H. Duan, Z. Pan, E. Hunter, A. H. Korayem, X. L. Zhao, F. Collins and J.G. Sanjayan,

Mater. Des., 92 (2016)571.
54. P. Duxson, A. Fernández-Jiménez, J. L. Provis, G. C. Lukey, A. Palomo and J. S. van Deventer, *J. Mater. Sci.*, 42 (9) (2006) 2917.
55. T. Suwan, M. Fan and N. Braimah, *Mater. Chem. Phys.*, 180 (2016) 219.
56. Shaikh FUA, *Mater. Des.*, 50 (2013) 674.
57. J. Tailby and K. J. D. MacKenzie, *Cem. Concr. Res.*, 40 (5) (2010) 787.
58. M. Zhang, T. El-Korchi, G. Zhang, J. Liang and M. Tao, *Fuel.*, 134 (2014) 315.